

Chapter 7

Application: Compressible Multi-fluid Flows



Multi-fluid flows involving shock-accelerated inhomogeneities and shock-induced instability play essential roles in a wide variety of problems including, but not limited to, supersonic combustion [1], inertial confinement fusion [2], and supernova explosion [3]. Numerical simulations of these complex flows prove to be challenging in the presence of moving and deformable material interfaces, especially for fluids with large differences in their densities or thermodynamic properties. Therefore, a discontinuity-capturing, mass-conserving, and positivity-preserving scheme is desirable for compressible multi-fluid simulations.

Qamar et al. [4] implemented the CESE method of Chang [5] and Zhang et al. [6] for solving the one- and two-dimensional compressible two-fluid models of Kreeft and Koren [7]. Numerical simulations were performed for gas–liquid Riemann problems and interactions of air shock waves with inhomogeneities containing lighter and heavier gases. In comparison with the non-oscillatory central scheme [5] and the kinetic flux-vector splitting scheme [8], the CESE scheme gives better resolution of discontinuities. Because of its outstanding ability for discontinuity capturing, the studies on Richtmyer–Meshkov instability (RMI) [9, 10] and Rayleigh–Taylor instability (RTI) [11, 12] have greatly benefited from the development of this method. Those numerical results not only eliminated disturbing factors in experiments (e.g., dimensional effect, boundary effect, liquid mist scattering), but also provided more ideal working conditions (that cannot be easily realized in experiment) and more flow details (that cannot be timely recorded by camera).

Recently, the upwind time–space CESE method was used extensively in studies of shock-accelerated inhomogeneous flows [13–15] and RMI [16–18]. The compressible two-fluid flows are described by a volume-fraction-based five-equation model [19] coupled with the stiffened gas equation of state [20]. Extensive numerical simulations were carried out using the maximum-principle-satisfying upwind CESE scheme [13], which is an improved version of the upwind CESE scheme presented in Chap. 4. The maximum-principle satisfying property is achieved by adopting a very simple limiter proposed by [21]. Furthermore, the ability to capture contact discontinuities

(material interfaces) can be enhanced by employing the HLLC Riemann solver in the upwind procedure. As a result, challenging numerical simulations of the gas–gas and gas–liquid Riemann problems were successfully performed, in which the mass of each fluid component is conserved and the positivity of volume fractions is preserved [13].

In this chapter, we use extensive numerical examples to indicate that the CESE method captures shocks and contact discontinuities sharply without spurious oscillations and proves to be a robust and accurate numerical tool for studies of compressible multi-fluid flows.

7.1 Richtmyer–Meshkov Instability

The Richtmyer–Meshkov instability occurs when an initially perturbed interface separating two different fluids is impulsively accelerated. This impulsive acceleration, in RMI studies especially, is provided by shock waves mostly. Two basic mechanisms dominate the RMI development, are the baroclinic vorticity and the pressure disturbance. For the baroclinic vorticity, the extent of the misalignment of the pressure gradient across the shock with the density gradient across the material interface makes contribution to the perturbation growth. While for the pressure disturbance, the wave system plays an important role.

As the inertial confinement fusion (ICF) cares more about the interaction of a converging shock with a disturbed interface, the converging RMI has become an imperative [22, 23]. The nature of geometrical convergence in converging RMI, however, makes the perturbation development more complicated because of the coupling of the Bell–Plesset (BP) effect [24, 25], Rayleigh–Taylor (RT) effect [26, 27], and the multiple shock impacts therein.

In perfect agreement with their experimental images [28], Zhai et al. [17] used the upwind CESE method to make further discussion about the converging RMI issues. Figure 7.1 shows the shock behaviors and interface morphologies after a converging shock interacting with perturbed interface. The inner test gas is SF₆ and the interface initial amplitude is 1 mm. The comparison clearly approved the applicability of the method used in simulating converging shock waves and converging RMI issues.

The Rayleigh–Taylor effect on the phase inversion (RTPI) was the major concern in Zhai’s work [17], which is supposed to be helpful in finding a freezing state interface in ICF physics. In this work, the influence of the initial amplitude on the RTPI was firstly investigated. Figure 7.2 depicts three converging RMI cases with different initial amplitudes (Cases I1, I2 and I3 with $a_0 = 1.0, 1.65,$ and 2.0 mm, respectively), according to which, Fig. 7.3 records the time-variation of the interface amplitudes. It was found that the amplitude histories can be roughly segmented into three stages after the initial shock compression. At the first stage, the amplitude of the perturbed interface increases because of the RMI, while during the second stage before re-shock, the amplitude reduces owing to the RT stabilization effect which is caused by the stronger adverse pressure gradient near the geometry origin. Based

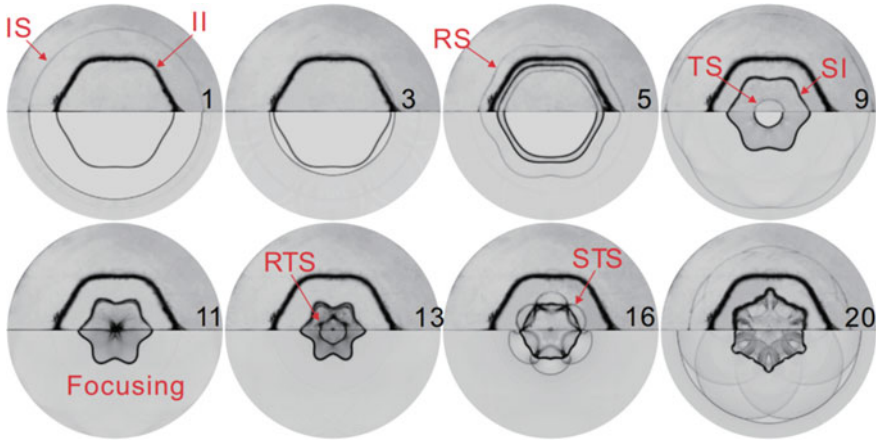


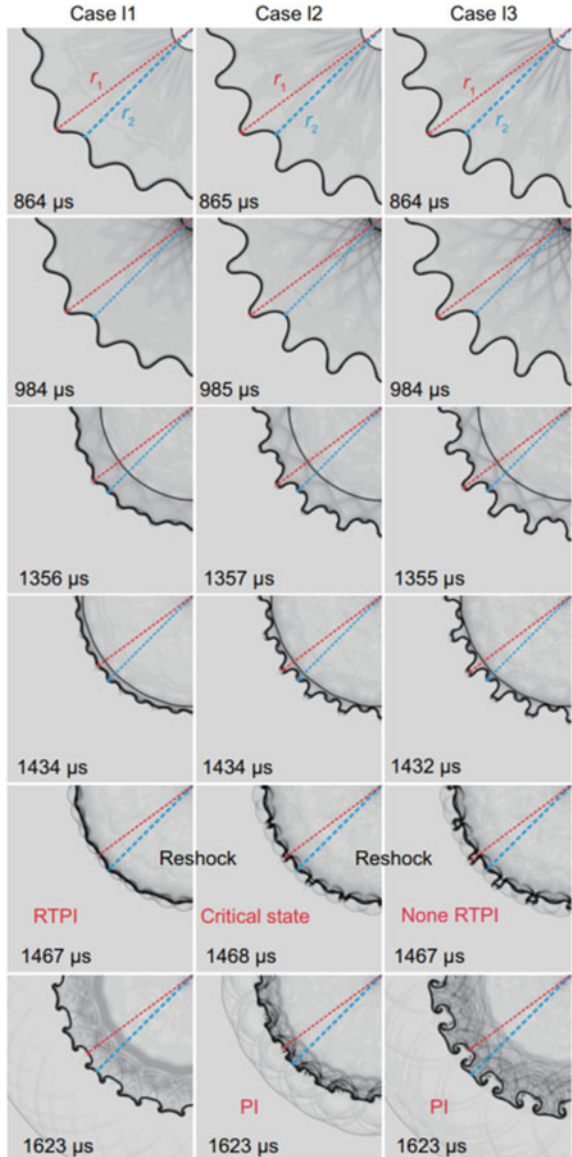
Fig. 7.1 The evolution of a single-mode interface with initial amplitude 1 mm. upper: experimental schlieren image; lower: numerical schlieren image at the same instants. (IS = incident shock, II = initial interface, RS = reflected shock, TS = transmitted shock, SI = shocked interface, RTS = reflected transmitted shock, STS = secondary transmitted shock). Courtesy of Z. G. Zhai [17]

on the amplitude histories, they concluded that whether a normal phase inversion occurs or not depends on the competition between the RT stabilization effect and RM instability caused by the re-shock. Especially, for a special initial amplitude, there is a critical state with a zero-amplitude of the interface at the re-shock.

Furthermore, a parametric study was performed to evaluate the influences of Atwood number, shock Mach number, and initial radius of the interface on the variation of critical amplitude with the azimuthal mode number. Their thorough investigation well explained the reason why this sensitive RTPI phenomenon was not observed in previous converging RMI studies.

The even more complicated converging RMI at a dual-mode interface was numerically studied by Zhou et al. [18] using the same upwind CESE methodology. It is not surprising that the dual-mode or multi-mode interface is far more complicated than the single-mode converging counterpart due to the existence of mode interferences such as harmonic generation and bubble merger. By comparing the detailed processes of the interface deformation and wave propagation for different dual-mode cases together with the development of a referencing single-mode interface, significant influence of the phase difference between two basic waves on the instability development can be clearly distinguished. While after the re-shock, the discrepancy becomes much smaller due to the weak dependence of the re-shocked RMI on the pre-re-shock state.

Fig. 7.2 Schlieren images showing the evolution of the single-mode interface. (PI = phase inversion, RTPI = Rayleigh–Taylor phase inversion). Courtesy of Z. G. Zhai [17]



The study on dynamics of the dual-mode converging RMI clearly reveals the mode coupling effect, in which the growth of the first mode was found to be inhibited, promoted, or not influenced, depending upon the first mode amplitude as well as the phase difference between the two basic waves. These findings, including all the other parametric studies in their work [18], were considered to be of great help for designing an optimal structure of the ICF capsule.

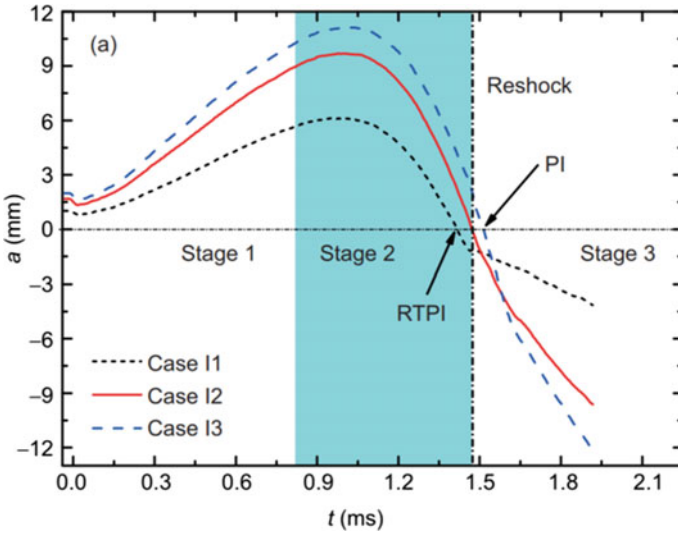


Fig. 7.3 Time-variation of interface amplitude in three perturbed cases. (PI = phase inversion, RTPI = Rayleigh–Taylor phase inversion). Courtesy of Z. G. Zhai [17]

7.2 Rayleigh–Taylor Instability

Other than the shock-induced interface instability, the rarefaction-induced instability was performed by [29] using the upwind space–time CESE method. Some of their numerical schlieren images of the SF₆/air interface instabilities induced by the rarefaction waves are presented in Fig. 7.4, in which the rarefaction waves were generated by simulating a diaphragm burst in a SF₆ shock tube. The influence of rarefaction wave acting time was demonstrated by varying the distance between the initial diaphragm and the gas interface (shown in cases SA1, SA3, and SA5); while the influence of the rarefaction wave strength was demonstrated by setting different pressure ratios between the two sides of the initial diaphragm (shown in SA3, SA7, and SA9).

Generally, after the rarefaction wave sweeps the SF₆/air interface from the down-side, RTI is triggered and the perturbation on the interface gradually grows. Different from the classical RMI where an impulsive action is exerted, and also different from the classical RTI where a continuous body force exists, the rarefaction wave imposes acceleration to the interface within a limited time. When the rarefaction wave leaves the interface, the baroclinic vorticity dominates the later interface evolution and KHI occurs on the interface as the further stretching of spikes and bubbles.

Based on the numerical results provided by the upwind CESE method, theoretical models were modified in Liang’s work [29] considering the time-varying acceleration and the growth rate transition from RTI to RMI. It was also found that the interface perturbation can be more unstable under the rarefaction wave condition than under

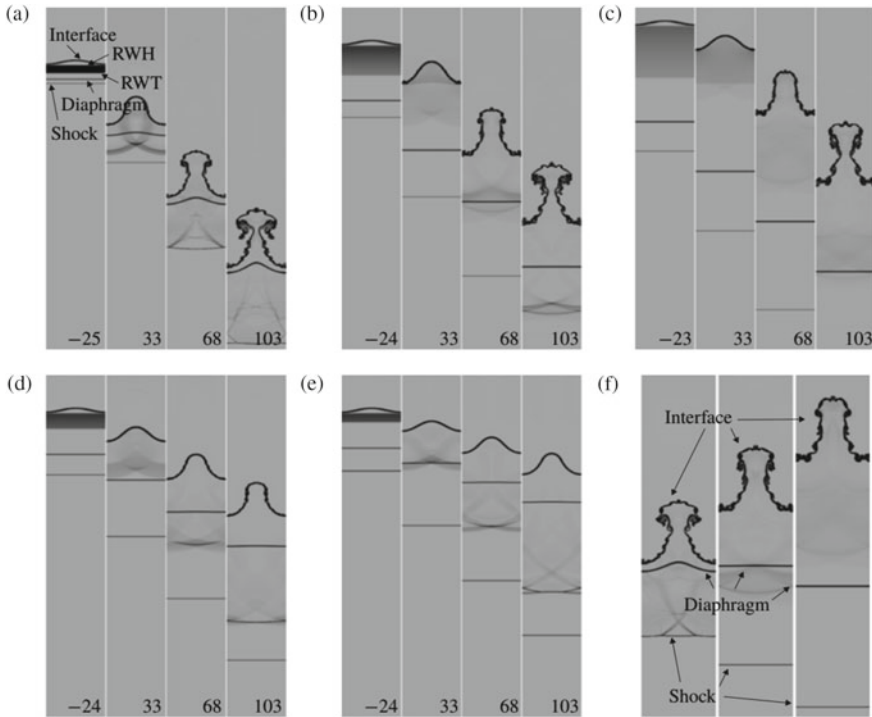


Fig. 7.4 Schlieren images of the SF₆/air interface evolution induced by rarefaction waves in cases **a** SA1, **b** SA3, **c** SA5, **d** SA7, and **e** SA9. Numbers represent the time in μs . **f** schlieren images of the interface evolution in cases SA1 (left), SA3 (middle) and SA5 (right) at dimensionless time 10.3. (RWH = rarefaction wave head, RWT = rarefaction wave tail). Courtesy of Y. Liang [29]

the shock wave condition due to the larger amount of vorticity deposited by the continuous pressure gradient.

7.3 Shock Refraction

The upwind space–time CESE method has also been used in simulating the shock refraction phenomenon at an inclined air/helium interface in the cylindrical converging shock scenario [16]. Figure 7.5 presents the experimental and numerical schlieren images of the shock refraction, in which good agreement between the two was achieved. Moreover, the numerical results apparently provide much cleaner images than their experimental counterparts (especially the region behind the deformed gas interface).

It is observed that, during the incident shock wave converging, when the shock velocity increases and the incident angle (with respect to the gas interface) decreases,

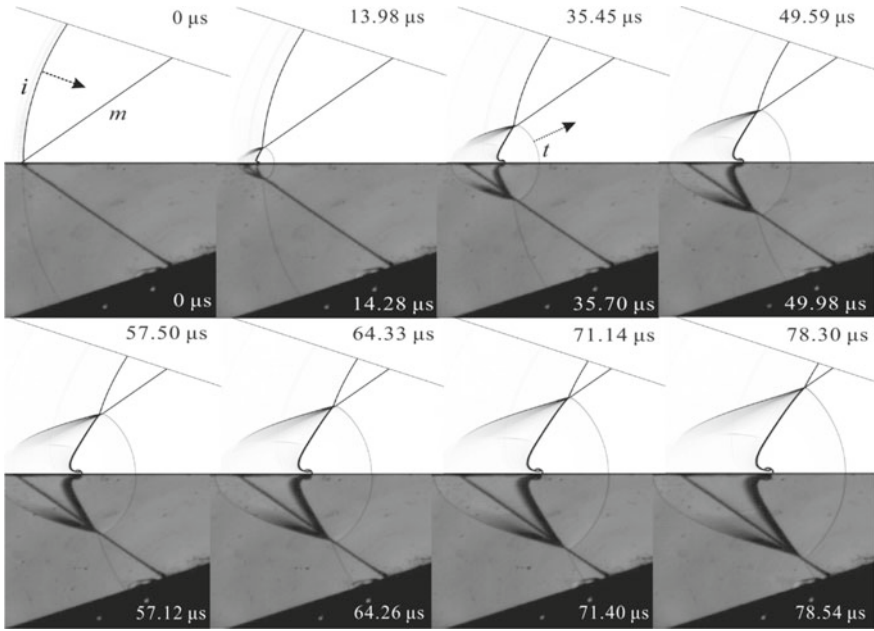


Fig. 7.5 Sequences of experimental (lower) and numerical (upper) schlieren frames showing the evolution of a converging shock wave refracting at a 45° tilted interface. (*i* = incident shock, *m* = material interface, *t* = transmitted shock). Courtesy of Z. G. Zhai [16]

the wave pattern is found to transit from one to another. In the work of Zhai et al. [16], two interfaces with 45° and 60° initial incident angles were examined. For the 45° case, the shock pattern was found to transit from free precursor refraction (FPR) to bound precursor refraction (BPR), and then to regular refraction with reflected shock (RRR); while for the 60° case, it was found to be from twin von Neumann refraction (TNR), to twin regular refraction (TRR), to free precursor von Neumann refraction (FNR), and finally to FPR. These clearly depicted transition sequences that never occur in the planar shock scenarios, greatly enriched the shock refraction classification.

7.4 Shock–Gas-Bubble Interaction

Here, we review the numerical studies of shock-accelerated inhomogeneous flows conducted by Shen et al. [13], Fan et al. [15], and Guan et al. [14] first. Figure 7.6 shows a general schematic of the computational setting of a shock-accelerated inhomogeneity. The homogeneity can be gas bubble [13], water column [13] or droplet [14], and the shape of the initial homogeneity can be circular, square, rectangular, and even triangular [15].

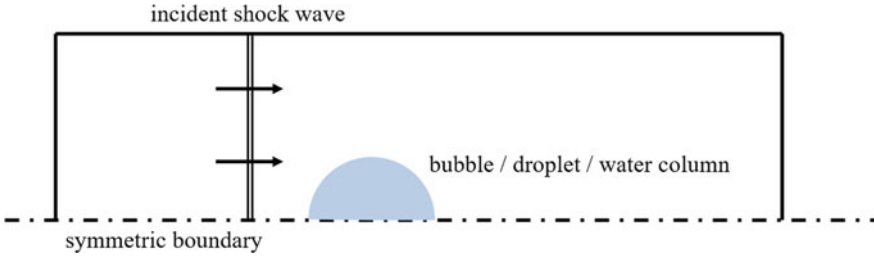


Fig. 7.6 Schematic of the initial setup for the interaction of an incident shock wave and a gas/water inhomogeneity

In the shock–helium–cylinder case [13], a planar shock propagates from left to right at Mach 1.22 and impacts the helium cylinder with a radius of 25 mm. The cylinder morphology after shock impact is shown in Fig. 7.7, in which the gas interface is sharply captured. The vortices, deposited due to baroclinicity, are clearly seen developing on the interface. As is shown, a salient feature of the helium cylinder morphology is the piercing of a middle air jet that finally separates the whole cylinder into two symmetric lobes.

A quantitative validation of the CESE method in simulating the shock–helium–cylinder interaction was performed by comparing the trajectories of the upstream point, the jet point, and the downstream point of the helium cylinder with the ones obtained by the level set method [30]. Good agreement of the results was achieved between the two methods, as depicted in Fig. 7.8.

The maximum-principle-satisfying upwind CESE scheme was applied by Fan et al. [15] to present a comprehensive study of jet-formation phenomenon in the interaction of a planar shock with a variety of heavy gas inhomogeneities. Comparing with the above light helium cylinder scenario, the heavy R22 cylinder experiences an obvious different deformation pattern. Figure 7.9 shows the cylinder morphology of the R22 cylinder with a radius of 25 mm impacted by a planar incident shock with Mach number 1.22 (to numerically reproduce the experiment conducted by Haas and Sturtevant [31]). The shocks that transmitted into this heavy cylinder were found converging at the downstream pole. The ensuing shock pattern and pressure gradient leads to a jet at the downstream cylinder surface.

Fan et al. [15] summarized that the heavy gas jet forms not only in the scenario of circular cylinder, but also in a series of differently shaped heavy gas cylinders, including square, rectangle, and triangle. Fan’s square case reproduced the experiment performed by Luo et al. [32] where the shock Mach was 1.17 in air and the side length of the SF₆ square was 56.6 mm. To reveal more details of the shock converging patterns in a small region, a slightly over-fined mesh was used in their simulation, which greatly reduced the numerical viscosity, making the secondary vortices at the late stage more pronounced than its corresponding experimental images. Other than that, numerical results shown in the lower halves of Fig. 7.10 agree quite well with the upper halves’ experimental images, including the gas interface morphology, the shock patterns, and the consequent jet formation at the middle leeward surface of

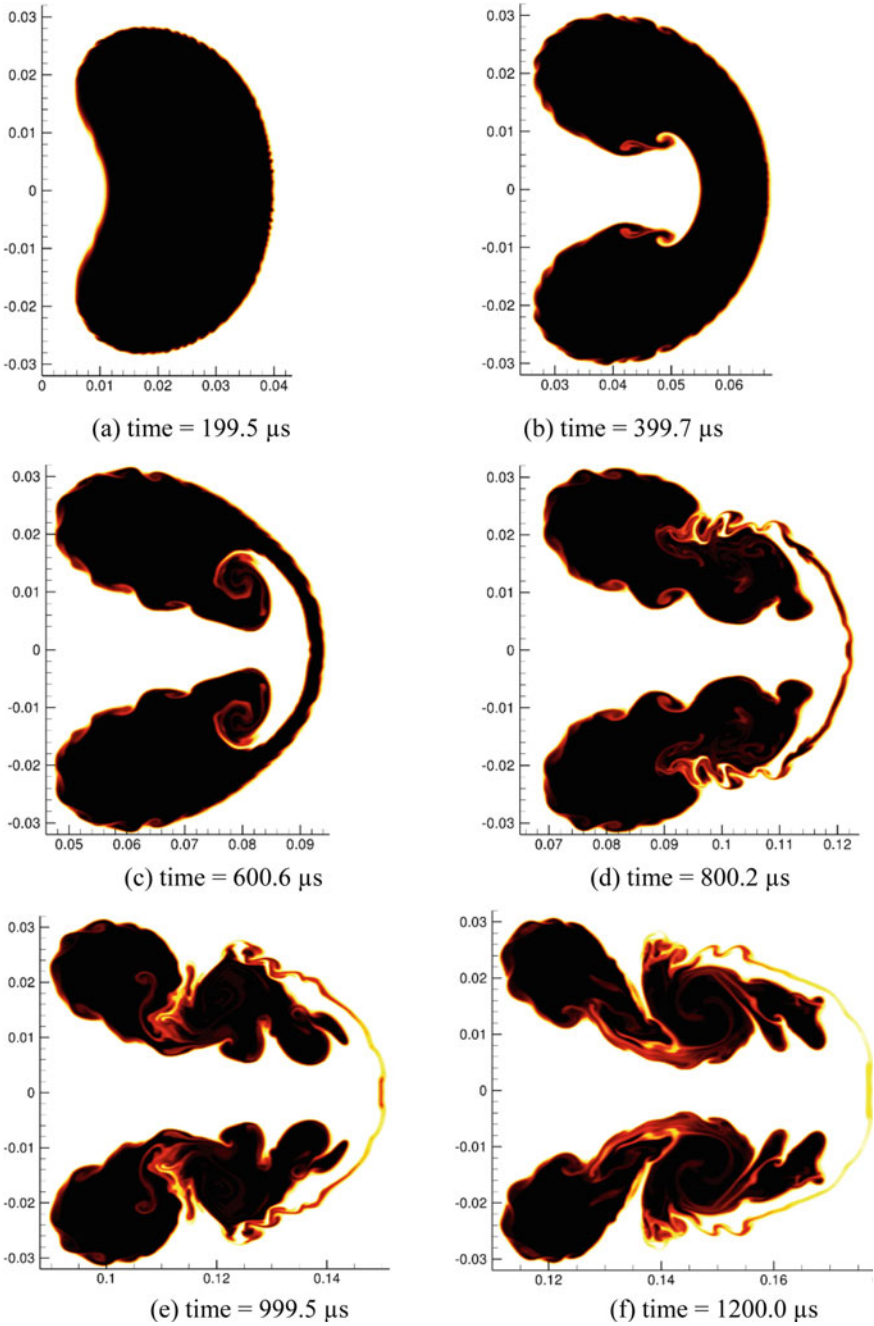


Fig. 7.7 Deformation history of a helium bubble impacted by a Mach 1.22 shock. Courtesy of H. Shen [13]

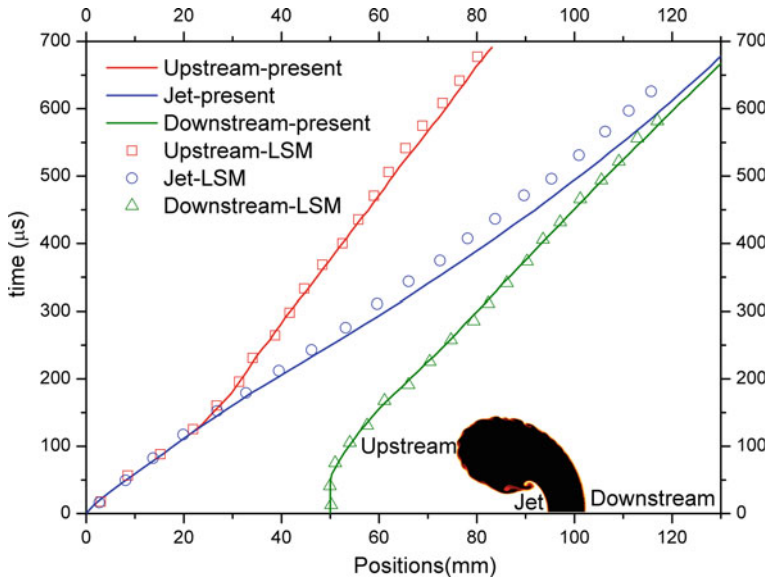


Fig. 7.8 Position history of the upstream point, the jet point, and the downstream point of the helium bubble. Courtesy of H. Shen [13]

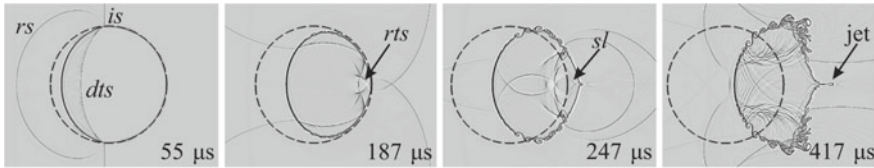


Fig. 7.9 Shadowgraphs of the evolution of an R22 circular cylinder under the impact of an incident shock with Mach number 1.22. (*is* = incident shock; *dts* = direct transmitted shock; *rs* = reflected shock; *rts* = reversed transmitted shock; *sl* = slip line.) Courtesy of E. Fan [15]

the square. Based on the detailed information provided by the CESE simulation, the mechanism of jet formation was revealed. It was found that for all the cases they simulated, the key factor in forming a downstream jet is the formation of type II shock-shock interaction [33]. According to this, a geometrical criterion was proposed to determine whether a jet will be formed [15].

7.5 Shock–Water-Droplet Interaction

The ability of the upwind CESE method to handle gas–liquid interfaces was initially demonstrated in Shen’s work [13]. The setup of this problem resembles that of the shock–bubble interaction (see Fig. 7.6). Due to the high-density ratio and large difference between the thermodynamic properties of air and water, more challenges

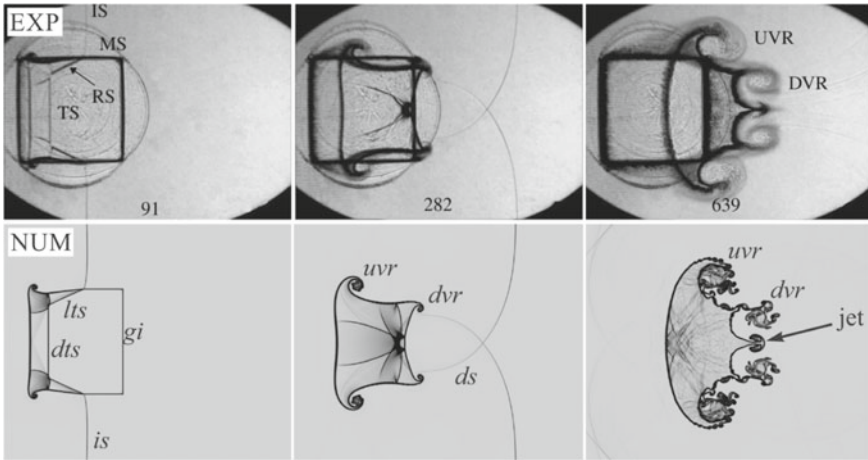


Fig. 7.10 Comparison of experimental images (upper) by Luo et al. [32] and the numerical results (lower) of the planar incident shock impact on a square cylinder using CESE method. (*is* = incident shock, *rs* = refracted shock, *ts* = transmitted shock, *ms* = Mach stem, *gi* = gas interface, *dts* = direct transmitted shock, *lts* = lateral transmitted shock, *ds* = diffracted shock, *uvr* = upstream vortex pair, *dvr* = downstream vortex pair). Courtesy of E. Fan [15]

are there in simulating the shock–water-column interaction. In this case, the radius of the water column was 2.4 mm and a shock wave with Mach number 1.47 was launched to sweep over the column from left to right. Upon the interaction of a shock with water column (or water droplet), two essential issues are extensively discussed. One issue concerns the immediate interaction of the shock wave (or rarefaction wave) with the water column (or droplet). It covers an extremely short period of time compared to the whole water column breakup, in spite of its vital role in the following interface deformation. The other issue concerns the long-period water column deformation, which covers from the initial protrusion growth on the water column surface to the later large interface distortion and mass loss of the bulk of the column. At the early stage, as shown in Fig. 7.11, the shock propagates through the water column as though passing over a rigid cylinder, nearly no interface deformation is detected. However, the shock waves as well as rarefaction waves bounce back and forth inside the water column, making the internal pressure change dramatically and becomes highly heterogeneous. After the incident shock has passed, as shown in Fig. 7.12, atomized water is gradually stripped away by the high-speed post-shocked flow. The water column develops into a crescent shape and the downstream was covered up by the transversely spreading atomized water. Note that the instabilities were captured in detail in this CESE simulation. The history of drag coefficient of the water column was also derived from the numerical results, as shown in Fig. 7.13. Again, good agreement was obtained in comparison with numerical simulations of Chen [34] and experimental data of Igra and Takayama [35].

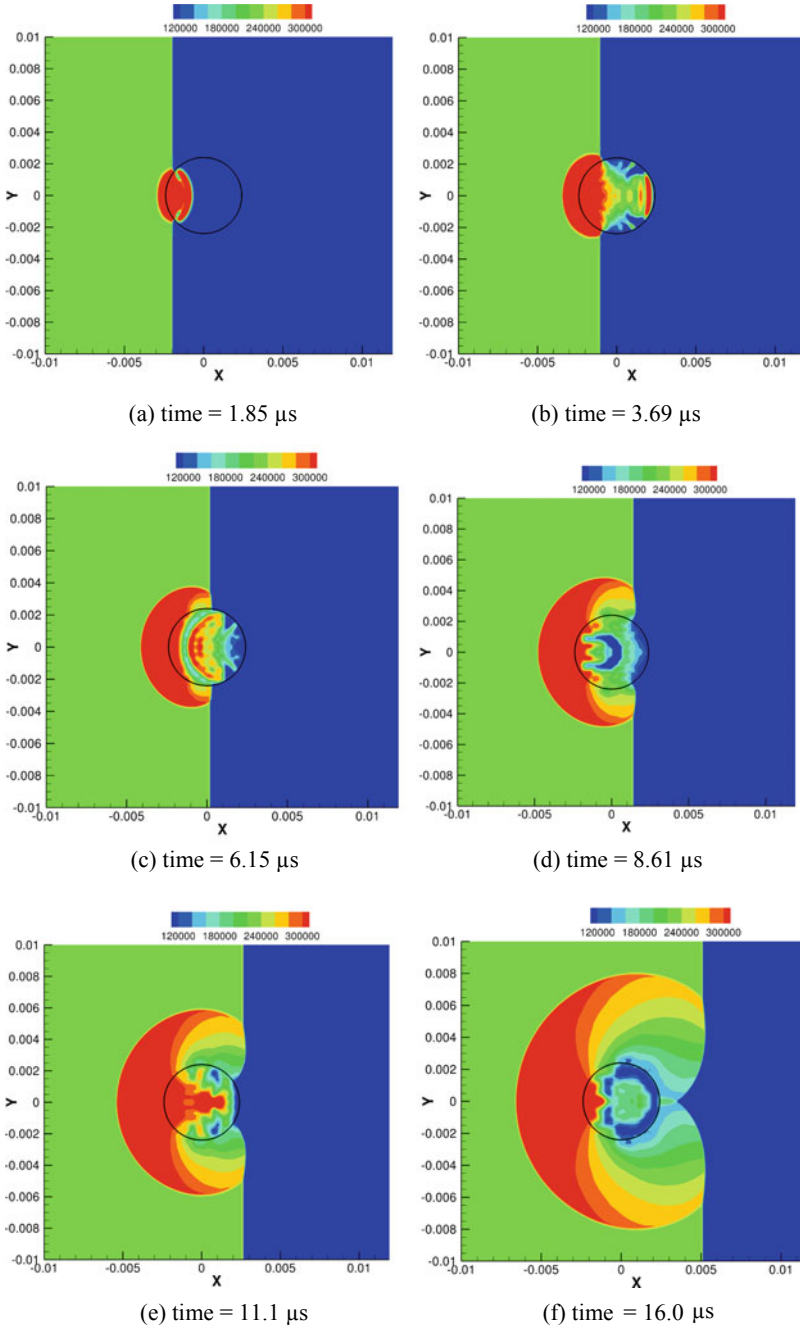


Fig. 7.11 Sequences of pressure contours (unit: Pa) in the early stage of a shock–water-column interaction. Courtesy of H. Shen [13]

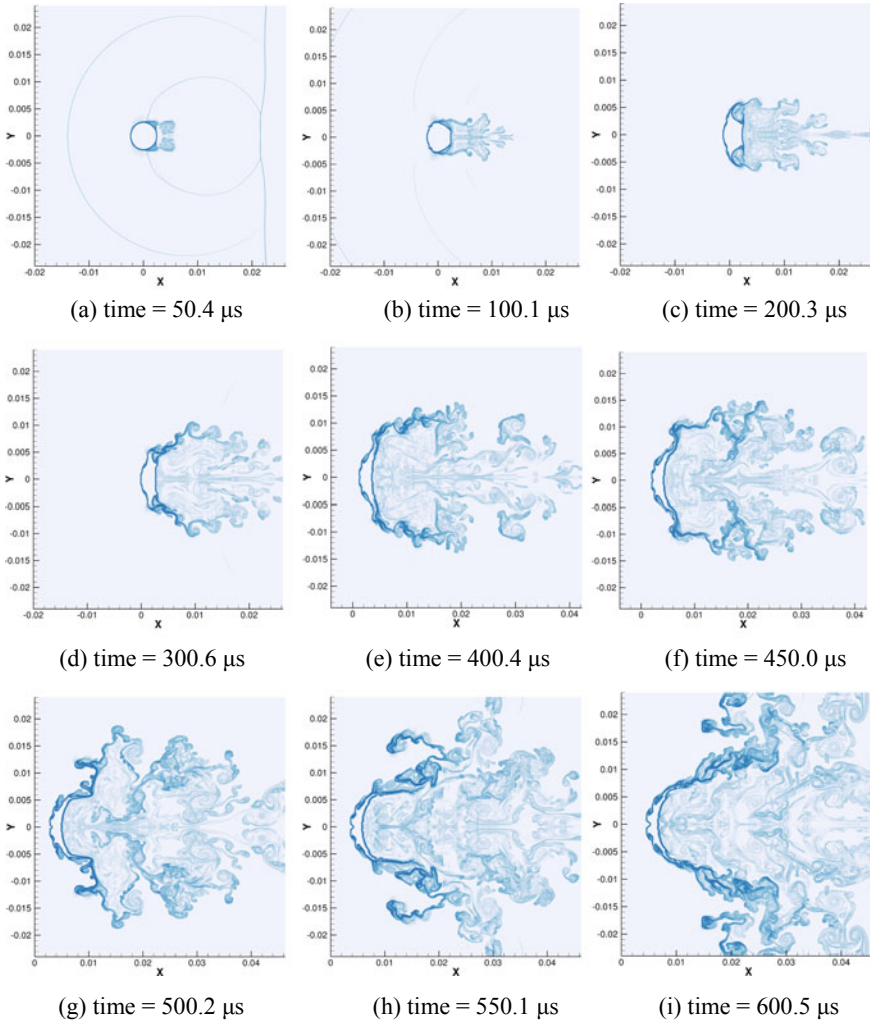


Fig. 7.12 Evolution of the numerical schlieren plot during the stripping breakup of the water column. Courtesy of H. Shen [13]

The case of a spherical water droplet deformation under planar shock impact was studied by Guan et al. [14] using axisymmetric simulation. As shown in Fig. 7.14, the initial protrusions emerging on the droplet surface were clearly captured by the CESE methodology. The internal flow pattern of the droplet was visualized numerically in this study. It is seen in Fig. 7.15 that the internal flow pattern of the droplet is established soon after the impact by the incident shock and is held steady for a long

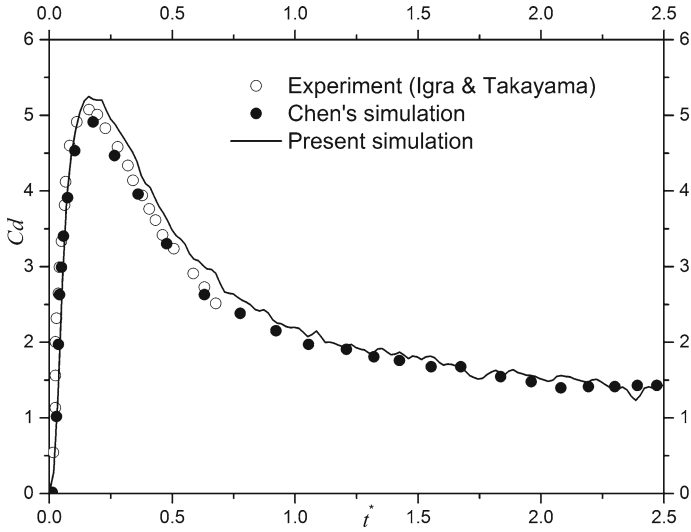


Fig. 7.13 Drag coefficient C_d history of a water column impacted by a shock versus dimensionless time t^* . Courtesy of H. Shen [13]

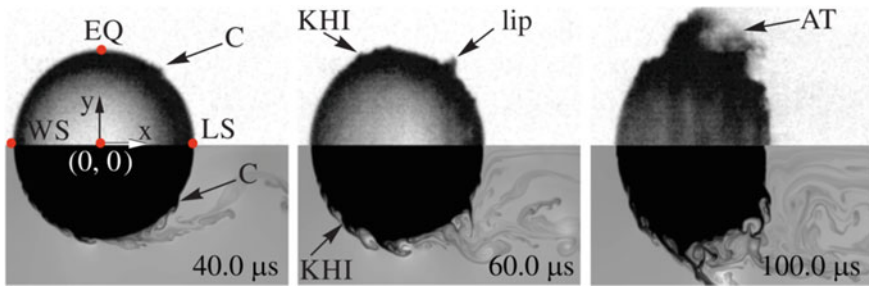


Fig. 7.14 Comparison of the numerical (lower part) and experimental (upper part) results at different instants. (EQ = equator; WS = windward stagnation; LS = leeward stagnation; C = corrugation; KHI = Kelvin-Helmholtz instability, AT = atomization). Courtesy of B. Guan [14]

time. For the first time, a saddle point was observed in this internal flow pattern. Further, a simple theory was proposed to correlate the stationary position of the saddle point with the Mach number of the incident shock.

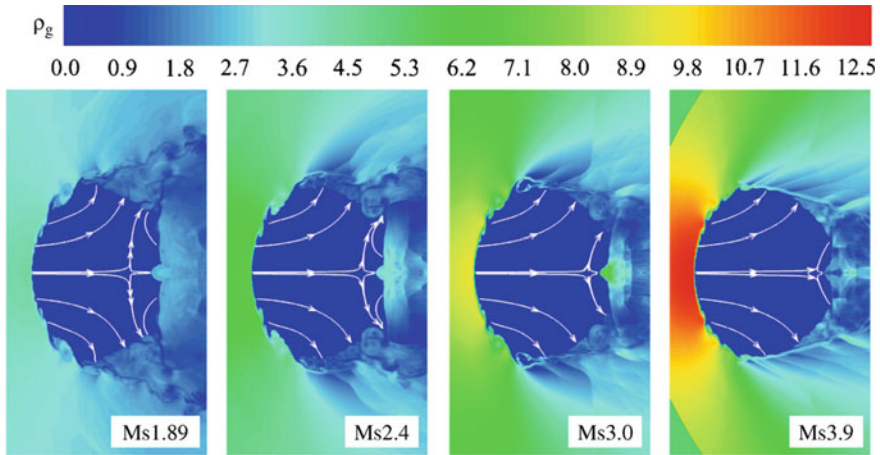


Fig. 7.15 Morphologies and internal flow patterns of a water droplet under shock impact with different shock Mach numbers Ms . Contours show the density of air with units kg/m^3 . Courtesy of B. Guan [14]

References

1. Park, S. J., Yu, S. T., Lai, M. C., Chang, S. C., & Jorgenson, C. (1999). Numerical calculation of unstable detonations by the method of space-time conservation element and solution element. In *37th Aerospace Sciences Meeting and Exhibit*.
2. Lindl, J., Landen, O., Edwards, J., Moses, E., & Team, N. (2014). Review of the national ignition campaign 2009–2012. *Physics of Plasmas*, 21(2), 020501.
3. Shimoda, J., Inoue, T., Ohira, Y., Yamazaki, R., Bamba, A., & Vink, J. (2015). On cosmic-ray production efficiency at supernova remnant shocks propagating into realistic diffuse interstellar medium. *The Astrophysical Journal*, 803(2), 98.
4. Qamar, S., Ahmed, M., & Ali, I. (2012). The space-time CE/SE method for solving reduced two-fluid flow model. *Communications in Computational Physics*, 12(4), 1070–1095.
5. Chang, S. C. (1995). The method of space-time conservation element and solution element—A new approach for solving the Navier-Stokes and Euler equations. *Journal of computational Physics*, 119(2), 295–324.
6. Zhang, Z. C., Yu, S. J., & Chang, S. C. (2002). A space-time conservation element and solution element method for solving the two- and three-dimensional unsteady Euler equations using quadrilateral and hexahedral meshes. *Journal of Computational Physics*, 175(1), 168–199.
7. Kreeft, J. J., & Koren, B. (2010). A new formulation of Kapila's five-equation model for compressible two-fluid flow, and its numerical treatment. *Journal of Computational Physics*, 229(18), 6220–6242.
8. Qamar, S., & Ahmed, M. (2009). A high order kinetic flux-vector splitting method for the reduced five-equation model of compressible two-fluid flows. *Journal of Computational Physics*, 228(24), 9059–9078.
9. Richtmyer, R. D. (1954). *Taylor instability in shock acceleration of compressible fluids*. Los Alamos Scientific Lab., N. Mex.
10. Meshkov, E. (1969). Instability of the interface of two gases accelerated by a shock wave. *Fluid Dynamics*, 4(5), 101–104.
11. Rayleigh. (1900). Investigation of the character of the equilibrium of an incompressible heavy fluid of variable density. *Scientific Papers*, 200–207.

12. Taylor, G. I. (1950). The instability of liquid surfaces when accelerated in a direction perpendicular to their planes. I. *Proceedings of the Royal Society of London. Series A. Mathematical and Physical Sciences*, 201(1065), 192–196.
13. Shen, H., Wen, C. Y., Parsani, M., & Shu, C. W. (2017). Maximum-principle-satisfying space-time conservation element and solution element scheme applied to compressible multifluids. *Journal of Computational Physics*, 330, 668–692.
14. Guan, B., Liu, Y., Wen, C. Y., & Shen, H. (2018). Numerical study on liquid droplet internal flow under shock impact. *AIAA Journal*, 56(9), 3382–3387.
15. Fan, E., Guan, B., Wen, C. Y., & Shen, H. (2019). Numerical study on the jet formation of simple-geometry heavy gas inhomogeneities. *Physics of Fluids*, 31(2), 026103.
16. Zhai, Z., Li, W., Si, T., Luo, X., Yang, J., & Lu, X. (2017). Refraction of cylindrical converging shock wave at an air/helium gaseous interface. *Physics of Fluids*, 29(1), 016102.
17. Zhai, Z., Zhang, F., Zhou, Z., Ding, J., & Wen, C. Y. (2019). Numerical study on Rayleigh–Taylor effect on cylindrically converging Richtmyer–Meshkov instability. *Science China Physics, Mechanics & Astronomy*, 62(12), 1–10.
18. Zhou, Z., Ding, J., Zhai, Z., Cheng, W., & Luo, X. (2020). Mode coupling in converging Richtmyer–Meshkov instability of dual-mode interface. *Acta Mechanica Sinica*, 36(2), 356–366.
19. Shyue, K. M. (1998). An efficient shock-capturing algorithm for compressible multicomponent problems. *Journal of Computational Physics*, 142(1), 208–242.
20. Saurel, R., & Abgrall, R. (1999). A simple method for compressible multifluid flows. *SIAM Journal on Scientific Computing*, 21(3), 1115–1145.
21. Zhang, X., & Shu, C. W. (2010). On maximum-principle-satisfying high order schemes for scalar conservation laws. *Journal of Computational Physics*, 229(9), 3091–3120.
22. Liang, Y., Zhai, Z., & Luo, X. (2018). Interaction of strong converging shock wave with SF6 gas bubble. *Science China Physics, Mechanics & Astronomy*, 61(6), 1–9.
23. Wu, Z., Huang, S., Ding, J., Wang, W., & Luo, X. (2018). Molecular dynamics simulation of cylindrical Richtmyer–Meshkov instability. *Science China Physics, Mechanics & Astronomy*, 61(11), 1–11.
24. Bell, G. I. (1951). Taylor instability on cylinders and spheres in the small amplitude approximation. Report No. LA-1321, LANL 1321.
25. Plesset, M. (1954). On the stability of fluid flows with spherical symmetry. *Journal of Applied Physics*, 25(1), 96–98.
26. Fincke, J., Lanier, N., Batha, S., Hueckstaedt, R., Magelssen, G., Rothman, S., Parker, K., & Horsfield, C. (2004). Postponement of saturation of the Richtmyer–Meshkov instability in a convergent geometry. *Physical Review Letters*, 93(11), 115003.
27. Lombardini, M., Pullin, D., & Meiron, D. (2014). Turbulent mixing driven by spherical implosions. Part I. Flow description and mixing-layer growth. *Journal of Fluid Mechanics*, 748, 85–112.
28. Luo, X., Zhang, F., Ding, J., Si, T., Yang, J., Zhai, Z., & Wen, C. Y. (2018). Long-term effect of Rayleigh–Taylor stabilization on converging Richtmyer–Meshkov instability. *Journal of Fluid Mechanics*, 849, 231–244.
29. Liang, Y., Zhai, Z., Luo, X., & Wen, C. Y. (2020). Interfacial instability at a heavy/light interface induced by rarefaction waves. *Journal of Fluid Mechanics*, 885, A42.
30. Terashima, H., & Tryggvason, G. (2009). A front-tracking/ghost-fluid method for fluid interfaces in compressible flows. *Journal of Computational Physics*, 228(11), 4012–4037.
31. Haas, J. F., & Sturtevant, B. (1987). Interaction of weak shock waves with cylindrical and spherical gas inhomogeneities. *Journal of Fluid Mechanics*, 181, 41–76.
32. Luo, X., Wang, M., Si, T., & Zhai, Z. (2015). On the interaction of a planar shock with an polygon. *Journal of Fluid Mechanics*, 773, 366–394.
33. Edney, B. (1968). Anomalous heat transfer and pressure distributions on blunt bodies at hypersonic speeds in the presence of an impinging shock, Flygtekniska Forsoksanstalten, Stockholm (Sweden).

34. Chen, H. (2008). Two-dimensional simulation of stripping breakup of a water droplet. *AIAA Journal*, 46(5), 1135–1143.
35. Igra, D., & Takayama, K. (2001). A study of shock wave loading on a cylindrical water column. *Report of the Institute of Fluid Science, Tohoku University*, 13, 19–36.

Open Access This chapter is licensed under the terms of the Creative Commons Attribution 4.0 International License (<http://creativecommons.org/licenses/by/4.0/>), which permits use, sharing, adaptation, distribution and reproduction in any medium or format, as long as you give appropriate credit to the original author(s) and the source, provide a link to the Creative Commons license and indicate if changes were made.

The images or other third party material in this chapter are included in the chapter's Creative Commons license, unless indicated otherwise in a credit line to the material. If material is not included in the chapter's Creative Commons license and your intended use is not permitted by statutory regulation or exceeds the permitted use, you will need to obtain permission directly from the copyright holder.

